

# Design Features and Mutual Compatibility Studies of the Time-of-Flight PET Capable GE SIGNA PET/MR System

Craig S. Levin\*, Sri Harsha Maramraju, Mohammad Mehdi Khalighi, Timothy W. Deller, Gaspar Delso, and Floris Jansen

**Abstract**—A recent entry into the rapidly evolving field of integrated PET/MR scanners is presented in this paper: a whole body hybrid PET/MR system (SIGNA PET/MR, GE Healthcare) capable of simultaneous acquisition of both time-of-flight (TOF) PET and high resolution MR data. The PET ring was integrated into an existing 3T MR system resulting in a (patient) bore opening of 60 cm diameter, with a 25 cm axial FOV. PET performance was evaluated both on the standalone PET ring and on the same detector integrated into the MR system, to assess the level of mutual interference between both subsystems. In both configurations we obtained detector performance data. PET detector performance was not significantly affected by integration into the MR system. The global energy resolution was within 2% (10.3% versus 10.5%), and the system coincidence time resolution showed a maximum change of < 3% (385 ps versus 394 ps) when measured outside MR and during simultaneous PET/MRI acquisitions, respectively. To evaluate PET image quality and resolution, the NEMA IQ phantom was acquired with MR idle and with MR active. Impact of PET on MR IQ was assessed by comparing SNR with PET acquisition on and off. B0 and B1 homogeneities were acquired before and after the integration of the PET ring inside the magnet. *In vivo* brain and whole body head-to-thighs data were acquired to demonstrate clinical image quality.

**Index Terms**—Simultaneous PET/MR, SiPMs, Time-of-Flight PET, scanner performance.

## I. INTRODUCTION

THE COMBINATION of MR and PET imaging modalities into a simultaneous hybrid system can be used for the assessment of biochemical processes in tissue, complemented with anatomical information with good soft-tissue contrast [1], [2]. The use of MR rather than CT as the anatomical complement to PET can lead to lower patient radiation dose and better soft tissue contrast. Simultaneous acquisition of PET and MR data creates opportunities to study processes with excellent spatial and temporal correlation between modalities. Further, the ability to use various MR pulse sequences provides greater tissue differentiation.

Manuscript received November 20, 2015; revised February 16, 2016; accepted February 17, 2016. Date of publication March 09, 2016; date of current version July 29, 2016. Asterisk indicates corresponding author.

\*C. S. Levin is with the Radiology and Molecular Imaging Program, Stanford University School of Medicine, Stanford, CA 94305 USA (e-mail: cslevin@stanford.edu).

S. H. Maramraju, T. W. Deller, and F. Jansen are with PET/MR Engineering, GE Healthcare, Waukesha, WI 53188 USA.

M. M. Khalighi is with the Applied Sciences Lab, GE Healthcare, Menlo Park, CA 94025 USA.

G. Delso is with the Applied Sciences Lab, GE Healthcare, 8006 Zurich, Switzerland.

Digital Object Identifier 10.1109/TMI.2016.2537811

Integrating PET and MRI in a single system capable of simultaneous operation is challenging. For true simultaneous imaging, the PET and MR components must be acquiring data from the same imaging volume; this means that unlike PET/CT, there is no option to physically offset one system relative to the other. This leads to a number of design constraints: lack of space, vibration, variable thermal load, and electromagnetic interference.

A vacuum photomultiplier (PMT) cannot operate in strong magnetic fields. The solution is either to move the PMT to a location where the magnetic field is weaker [3]–[5], or to replace it with a different photosensor [6]–[8]. Avalanche photodiodes (APDs) and, more recently, silicon photomultipliers (SiPMs), have allowed the development of PET detector designs with small footprint and capable of operating in strong magnetic fields. An APD-based hybrid brain PET/MR system was developed and used for neurodegenerative applications [9]. The first clinical PET/MR scanners that were introduced commercially include an APD-based non-time-of-flight (non-TOF) integrated system [10] and a PMT-based TOF sequential system [11]. A trimodality (TOF-PET/CT and MR) system with dedicated shuttle was also introduced to perform sequential PET/MR imaging [12].

Time-of-flight (TOF) PET technology can improve PET image quality—especially in larger patients [13]–[15]. Recent advances in TOF PET detectors have been made possible by the combination of fast bright scintillators coupled to fast, high gain photosensors with high photon detection efficiency [16]. In particular, SiPMs have proven to be suitable for TOF detectors as they combine high gain and low noise with magnetic insensitivity [17]. The present work describes the design and technical performance evaluation of a TOF-capable SiPM-based clinical PET detector that has been integrated with a 3T MR scanner. Specifically, we evaluated the impact of the PET detector ring on the performance of the MR system and vice versa, as well as the performance of the radiofrequency (RF) body coil. A full NEMA PET performance characterization and clinical evaluation are performed elsewhere [18], [19].

## II. MATERIALS AND METHODS

### A. PET/MRI System

The design of the integrated SIGNA PET/MR was based on the 3T MR750w MR scanner (GE Healthcare), a whole body

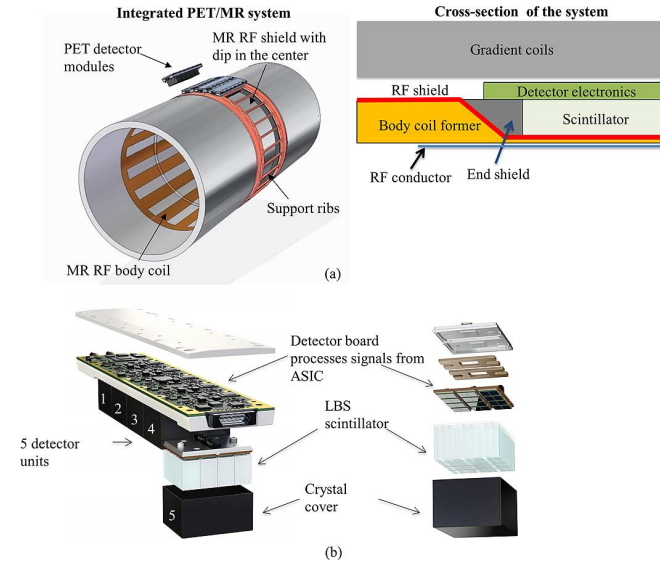


Fig. 1. (a) Schematic of the PET/MR integrated system, showing the cross-section of a detector integrated with the RF body coil; (b) Schematic of a detector module and unit.

MRI system with a 70 cm patient bore. The MR parts of the integrated design use the same superconducting magnet, gradient coils (amplitude 44 mT/m, maximum slew rate 200 T/m/s) and transmit/receive electronics as the original MR product. The RF body coil and RF shield were redesigned in order to accommodate the PET detector ring, and to shield it from the RF transmit power. The PET detector was placed between the RF shield and the gradient coil, with the RF body coil inside the PET ring. An inward dip in the RF shield (Fig. 1(a)) allows space for the PET detector and minimizes attenuation. The PET detector ring is 25 cm axially and 62 cm face to face.

The PET system is designed to operate in the MR environment. This environment creates challenges of (lack of) space, strong magnetic field, thermal stress, vibrations, and large electromagnetic fields (from RF and gradients). Whilst being robust to these environmental stresses, the PET system needs to be electromagnetically quiet to prevent interference with the low level signal detected by the MR. To achieve good electromagnetic isolation, a multi-layered approach to shielding was used. The only electrical connection to each module is through a double-shielded (braid plus foil) cable that carries power and timing clock over twisted pair wiring; all other communication and control takes place over dual optical fibers.

The PET detector ring comprises 28 identical water-cooled modules, with a total of 720  $3.95 \times 5.3 \times 25$  mm<sup>3</sup> lutetium based scintillator (LBS) crystals (per module) read by arrays of Hamamatsu SiPM devices (HPK S12044). The schematic of one detector module is shown in Fig. 1(b). Main characteristics of the system can be found in Table I.

Signals from the SiPM arrays are processed by Application Specific Integrated Circuits (ASICs) (ON Semiconductor) mounted on the same board. X, Z, energy and timing signals are generated for each block. A schematic of readout electronics is shown in Fig. 2. The timing pickoff for each event is achieved by a pulse shaping circuit that takes the sum signal of the block

TABLE I  
CHARACTERISTICS OF INTEGRATED TIME-OF-FLIGHT PET/MR SYSTEM.

Magnet type	3T Superconductor
Patient bore diameter (cm)	60
Axial FOV (cm)	25
PET crystal type	LBS
PET crystal dimensions (mm <sup>3</sup> )	3.95 x 5.3 x 25
Number of crystals	20160
Number of detector modules	28
PET Sensitivity	22.9 cps/kBq
PET transaxial spatial resolution (at 1 cm)	4.3 mm

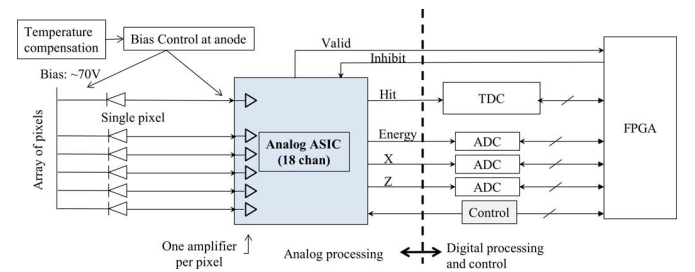


Fig. 2. Schematic of the front end data acquisition electronics of the PET system.

and feeds it to a fast comparator within the ASIC at a trigger level just above the noise (single photon) floor of the SiPM. Gain control is achieved with a common bias to the cathode, and differential bias to each anode (SiPM pixel).

Event processing takes place entirely inside the detector module: this includes digitization of time, position and energy, as well as corrections applied per crystal. Compton Scatter Recovery (CSR) detects scatter of 511 keV photons between adjacent detector blocks, and reconstitutes events in which the summed energy falls within the energy window [20]. The tight electronic integration and CSR are critical for maintaining the good timing resolution and sensitivity of the system.

Maintaining PET detector stability in the MR environment is challenging. During normal operation, the pulsing of the gradient coils induces eddy currents in the RF shielding, the detector housing, and the circuit boards. This represents a variable thermal load that depends on the pulse sequence used: this causes temperature fluctuations in the detector. By its design, an SiPM is sensitive to temperature changes. This sensitivity is addressed in several ways: first, the detector module is constructed to minimize induction of eddy currents. Next, a large ceramic cold plate (good thermal but poor electrical) is coupled to the module electronics, and is cooled with a constant flow of coolant (18°C). Finally, 280 thermistors measure temperature throughout the PET ring. The temperature map is used to generate a correction to the bias voltage applied to each individual anode, thus ensuring minimal gain drift [21]. In Fig. 3, we plot the mean system temperature measured as part of the daily quality assurance (DQA) scan, along with the mean singles and coincidence count rates obtained during the scan, for a

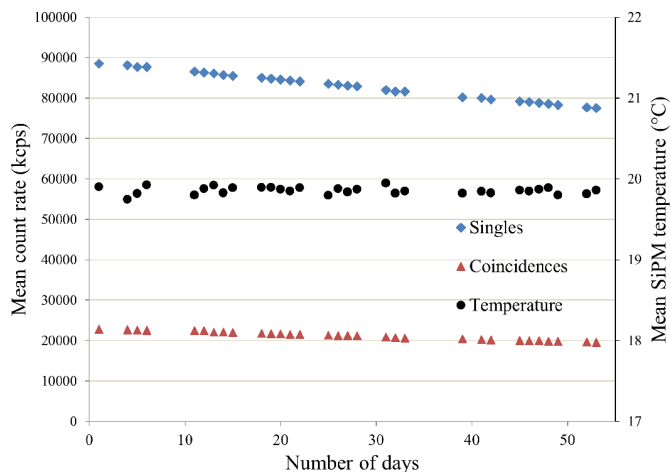


Fig. 3. Mean singles and coincidence count rate data collected during DQA scan each day for a total of 31 measurements. Mean system temperature is maintained between 19–20°C.

total of 31 separate measurements (weekends and holidays excluded). The gradual decline in count rates is due to the decay of the  $^{68}\text{Ge}$  source.

Another challenge encountered by the detector is gradient induced vibration. By mounting the PET detectors to the RF body coil, which is mechanically isolated from the gradient coil, these conducted vibrations are reduced.

### B. PET/MR Acquisitions

For PET/MR simultaneous scans, the user can prescribe standard MR clinical sequences to run concurrently with the PET acquisition. For every bed position, attenuation information is collected by acquiring an 18 second LAVA-Flex scan [22]. The PET photon attenuation coefficients at 511 keV are obtained by segmenting the Dixon images into air, lung, fat and water. Attenuation estimation is enhanced with an atlas-based registration for the head to include bone tissue [23]. A truncation completion algorithm [22], [24] uses the non-attenuation corrected TOF reconstructed PET image to estimate the patient outline; this outline is used to fill in information that is missing because of the limited field of view of the MR scanner (50 cm vs. 60 cm for PET).

Prior to any measurements, the PET detector was fully calibrated. Initial PET performance measurements were performed on a standalone ring before integrating it into the magnet. A 37 MBq  $^{68}\text{Ge}$  annulus phantom (12 cm outer diameter  $\times$  27 cm long) was positioned at the center of the bore to irradiate the PET detectors for initial scans. Flood histograms of the crystal map were acquired to identify crystal peak positions and assess whether any shifts occur when the detector ring is inside the magnet. Event data was acquired for 5 minutes to compute energy resolution—full width at half maximum (FWHM) of the relative position of the 511 keV photopeak. For timing resolution measurements, a 5.2 MBq  $^{68}\text{Ge}$  ceramic line source (0.15 cm inner diameter, 27 cm length) was positioned at the center of the bore. Timing resolution data was collected for 35 minutes.

TABLE II  
MR SCANNING PARAMETERS FOR PERFORMANCE MEASUREMENTS.

MR sequence	TR (ms)	TE (ms)	FOV (cm)	FA (°)
2-point Dixon	4	2	50	12
FRFSE	4765	102	22	140
GRE-EPI	1150	40	24	60

### C. Impact of MR on PET Performance

Three main conditions (standalone PET ring; with PET ring integrated in the magnet but with MR idle; and with PET ring integrated in the magnet with active MR pulsing), were considered to evaluate the impact of MR on PET performance. The effect of MR operation on PET performance was evaluated using the 2-point Dixon MR attenuation correction (MRAC) sequence, gradient recalled echo (GRE) echo-planar imaging (EPI) and fast recovery fast spin echo (FRFSE) pulse sequences, respectively. The parameters of these sequences are shown in Table II. The 2-point Dixon method was selected because it will be acquired with each clinical bed position for MRAC purposes.

The energy resolution and timing resolution measurements acquired using  $^{68}\text{Ge}$  annulus phantom and  $^{68}\text{Ge}$  ceramic pin source, respectively, were repeated with GRE-EPI and FRFSE sequences; these sequences were deliberately chosen for their high intensity RF (FRFSE) and gradients (GRE-EPI) pulsing conditions. The results that were obtained with the PET ring inside MR and with MR stimulus were then compared with the earlier measurements of the PET ring outside the magnet.

To further characterize the timing performance of the system, the timing resolution data was acquired as a function of activity. A flexible line source was filled with 161 MBq  $^{18}\text{F}$  (30 cm active length). The line was inserted into a 70 cm long aluminum tube and centered in the magnet, with the active region covering slightly more than the axial PET FOV. The scan time for each of the acquisitions was modified to acquire approximately 10 million true coincidences for each.

The impact of CSR [20] on PET sensitivity was investigated per the NEMA NU 2–2012 standard [25]. A 70 cm line source was filled with approximately 10 MBq of  $^{18}\text{F}$  and scanned along the central axis of the PET detector with one through five aluminum tubes (Data Spectrum Corporation (DSC), model PET/NEMA-SEN/P). For each number of tubes, data was acquired with CSR turned on (as in normal product operation) and with CSR turned off. Sensitivity measurements were extrapolated to a non-attenuating environment per the NEMA standard, and axial slice sensitivity profiles were generated.

To demonstrate the impact of MR sequences on PET image quality, the NEMA image quality phantom (DSC model PET/IEC-BODY/P) was filled with a 4:1 feature-to-background activity ratio. The background activity was filled to approximately 5.3 kBq/mL. Acquisition was performed with MR idle for the NEMA prescribed acquisition length (adjusted for activity concentration). Subsequent scans were acquired with simultaneous pulsing of the FRFSE and GRE-EPI sequence. The PET acquisition length for each of these subsequent scans was increased

to account for decay. The images were reconstructed using ordered-subset expectation maximization (OSEM) with 4 iterations, 28 subsets, 40 cm DFOV,  $256 \times 256$  image grid, 3 mm 2D Gaussian post-filter.

A registered CT scan of the same phantom was used for attenuation correction.

#### D. Impact of PET on MR

The impact of PET on MR was investigated in 3 stages. First, the performance of the 3T GE MR750w was evaluated before installing the PET “tube” comprising the PET ring and new RF body coil. Second, the evaluation was repeated with the PET ring integrated in the magnet and powered, but with PET acquisition idle. Finally, the measurements were repeated a third time while the system was acquiring PET data. The magnet was shimmed to the manufacturer's specification after the PET tube installation. The MR performance was evaluated by measuring the  $B_0$  homogeneity of the magnet and the  $B_1$  uniformity of the body coil, respectively. The functional bioinformatics research network (fBIRN) test [26] with head and body coil was used to determine the temporal stability of the magnet (for fMRI applications) as well as signal to noise ratio (SNR) and signal fluctuations to noise ratio (SFNR).

The  $B_0$  homogeneity was measured on 20, 30, 40 and 45 cm Diameter Sphere Volume (DSV) and peak and RMS of non-uniformity was measured. The  $B_0$  homogeneity was also measured with PET acquisition running. In addition, the  $B_1$  homogeneity of the Body coil was measured with the General Electric MR spectroscopy phantom [27] using Adiabatic Bloch Siegert  $B_1$ + mapping (ABS) [28] based on a conventional gradient echo sequence with the following parameters: 6 ms ABS pulse width, 5  $\mu$ T ABS pulse amplitude, 22 cm FOV, 5 cm thickness,  $64 \times 64$  matrix, 30 degree FA, 31.25 kHz Bandwidth, 100 ms repetition time (TR) and 9 ms echo time (TE). The  $B_1$  maps were scaled to reflect the maximum RF power available (35 kW RF Amplifier).  $B_1$  maps were collected 3 times for each of the three experimental configurations.  $B_1$ + average and  $B_1$ + homogeneity were compared between all 3 modes. The effect of PET acquisition on  $B_1$ + was evaluated by looking at the  $B_1$ + difference between (averaged)  $B_1$ + with and without PET acquisition.

To test the system stability for fMRI scans, the fBIRN test was performed on MRS phantom with Body transmit coil and two different receive coils (head-neck unit and Body coil). The test was repeated 3 times with the following parameters: Single Shot Echo Planar Imaging,  $64 \times 64$  matrix, 22 cm FOV, 3100 ms TR, 30 ms TE, 572  $\mu$ s echo spacing, 77 degree flip angle, 30 slices, 4 mm thickness, 1 mm spacing and 200 temporal phases. Slice number 15 was used to calculate system fluctuation, SNR and SFNR. Mean and standard deviation of each parameter were calculated using the 3 samples.

#### E. First Clinical Imaging Studies

To demonstrate clinical imaging performance of the system, a brain and a whole-body study were performed on two oncology patients at the University Hospital Zurich. The examinations were performed within the context of a clinical trial approved by the local clinical ethics committee. All patients provided written informed consent prior to the examination and were scanned

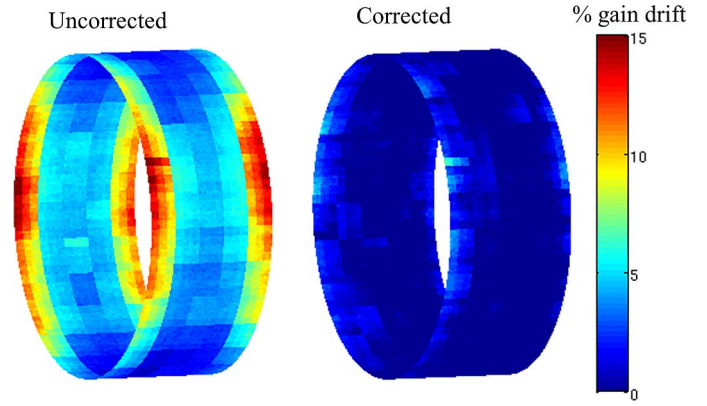


Fig. 4. PET ring map showing the percent gain drift during MR pulsing before applying gain drift correction (left) and after correction (right).

on the PET/MR system following a standard PET/CT exam, without additional tracer injection.

A 54-year old male subject with a history of abdominal lymphoma was administered 322 MBq of  $^{18}\text{F}$ -FDG. The indicated PET/CT protocol was acquired 60 minutes after injection. An additional brain PET/MR protocol was acquired 100 minutes after injection. MR and PET data were acquired simultaneously for 20 minutes. Various MR pulse sequences were acquired, including a 2-point Dixon MRAC and T2 axial FRFSE sequence (TR/TE = 8431/99 ms, flip angle =  $111^\circ$ , slice thickness = 4 mm). The brain PET data for PET/MR were reconstructed using 3D TOF OSEM (8 iterations, 28 subsets) with SharpIR point spread function (PSF) compensation, similar to the method described in [29]. The attenuation due to the presence of head coil was accounted for in PET reconstruction of the brain images.

For whole-body clinical study, a 61-year old woman having clinical indication of metastases in the lung and sternum regions, was administered with 178 MBq of  $^{18}\text{F}$ -FDG and was scanned on the PET/MR system, 77 minutes after FDG injection. A total of six bed positions were acquired for the whole-body study (5 minutes per bed position). The whole-body PET data for PET/MR were reconstructed using 3D TOF OSEM (2 iterations, 28 subsets). During PET reconstruction, the attenuation from head coil and patient cradle was accounted for in the attenuation map used.

### III. RESULTS

#### A. Scanner Performance Measurements

Fig. 4 shows the comparison of percent gain drift before and after gain drift correction. The mean gain shift over the entire system after gain correction is  $< 2\%$ .

Block crystal map plots outside of MR and during active MR RF pulsing are shown in Fig. 5. The mean PET energy resolution without MR stimulus is 10.3% FWHM. Table III shows the difference in mean system energy resolution over all measurements with and without MR is within 2%. In addition, there was minimal impact ( $< 3\%$ ) on timing resolution both outside MR and inside MR using various pulse sequences.

Fig. 6 shows mean timing resolution of all the crystals as a function of activity in the line source. In all cases, the fit is



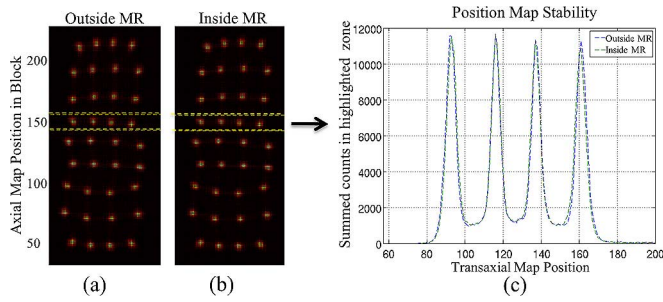


Fig. 5. Summed counts in PET crystal flood histogram of a single block (a) outside MR, (b) inside MR (FRFSE), (c) overlay of profile position through fourth row of the flood histogram for the same block inside and outside MR.

TABLE III  
COMPARISON OF ENERGY AND TIMING RESOLUTION WITH AND WITHOUT MR.

	Energy Resolution (%, FWHM)	Timing Resolution (ps)
<b>Outside MR (No MR coil in PET FOV)</b>	10.4	386
<b>Inside MR – MR Idle</b>	$10.3 \pm 0.00$	$385.3 \pm 0.07$
<b>Inside MR – FRFSE</b>	$10.5 \pm 0.02$	$394.1 \pm 0.06$
<b>Inside MR - 2D GRE EPI</b>	$10.5 \pm 0.02$	$388.9 \pm 0.14$

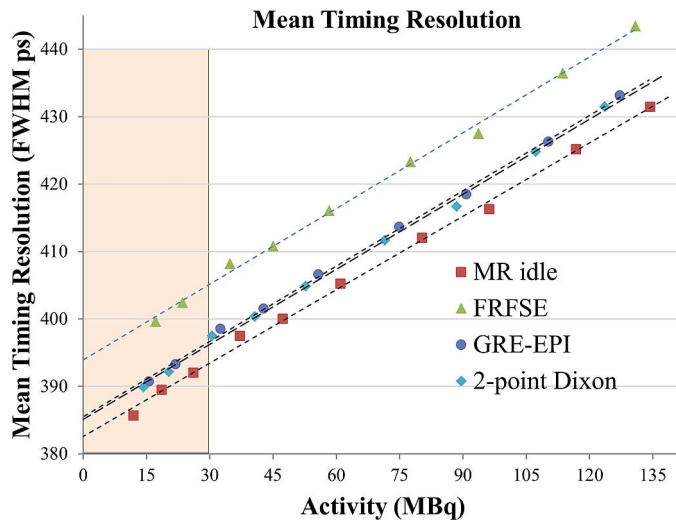


Fig. 6. Plot of mean coincidence time resolution for  $^{18}\text{F}$  using various MR pulse sequences and for MR idle. Timing resolution is minimally affected by MR pulse sequences and typical source strengths used for clinical studies (shaded region).

linear to within 0.3%. Fig. 7 shows comparison of PET sensitivity profile with and without CSR enabled. There is 18% gain in sensitivity with CSR enabled. PET images (Fig. 8) of the NEMA image quality phantom are visually similar and demonstrate minimal image degradation.

### B. Impact of PET on MR

Table IV shows the peak and RMS variations of  $B_0$  in 20, 30, 40 and 45 cm DSV between the 3 modes along with the manufacturer's specifications. It also shows that  $B_0$  homogeneity does not change with PET acquisition.

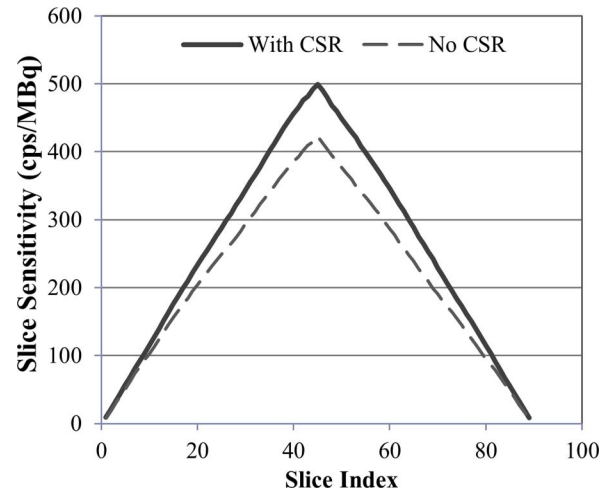


Fig. 7. Sensitivity profile comparison with CSR turned on (as in normal operation) compared to CSR turned off. The use of CSR provides an 18% increase in sensitivity.

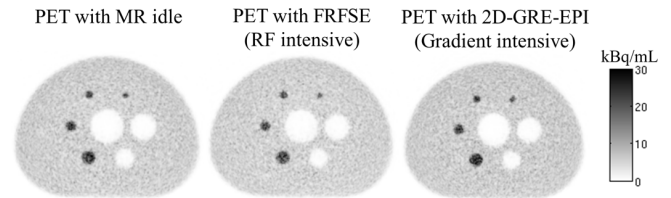


Fig. 8. PET images of NEMA IQ phantom with MR idle and MR active conditions.

TABLE IV  
 $B_0$  HOMOGENEITY COMPARISON.

DSV(cm)	45	40	30	20
<b>P-2-P MR750w, pre upgrade (ppm)</b>	8.32	2.51	0.88	0.39
<b>P-2-P PET/MR, No PET Acq.(ppm)</b>	11.35	3.81	1.06	0.39
<b>P-2-P PET/MR, with PET Acq.(ppm)</b>	11.58	3.91	1.10	0.39
<b>P-2-P Spec(ppm)</b>	15	6	2	1
<b>RMS MR750w, pre upgrade (ppm)</b>	0.45	0.20	0.10	0.05
<b>RMS PET/MR, No PET Acq. (ppm)</b>	0.52	0.25	0.12	0.05
<b>RMS PET/MR, with PET Acq. (ppm)</b>	0.51	0.25	0.12	0.05
<b>RMS Spec (ppm)</b>	1.25	1	0.5	0.1

Fig. 9(a) compares the  $B_1+$  maps between the 3 modes (Fig. 9(b) and (c)).

The  $B_1+$  uniformity remained the same between all modes; however, using the same transmit power, the  $B_1$  of the PET/MR Body coil is increased by 24% on average compared to MR750w, mainly due to the smaller size of the RF Body coil (60 cm vs. 70 cm diameter). Fig. 9(d) shows that the mean

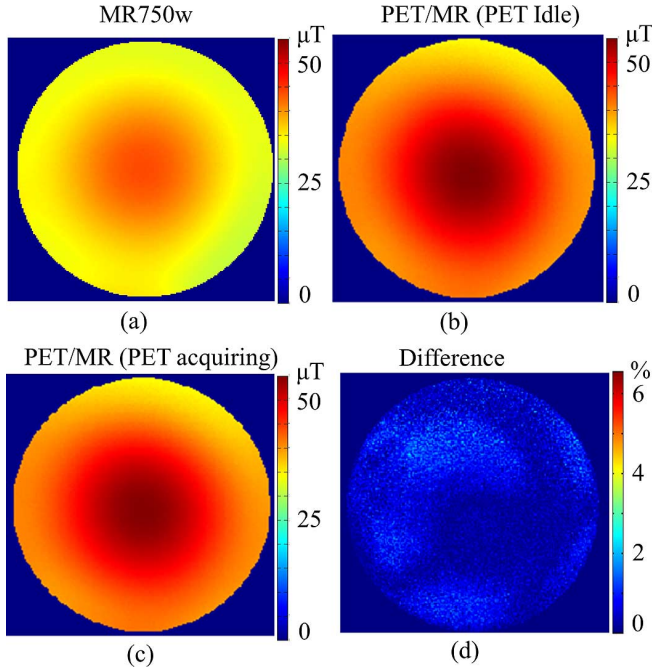


Fig. 9. Body coil B1 maps: (a) without PET ring (MR750w) with mean of  $37.1 \mu\text{T} \pm 10.2\%$ ; (b) after PET ring insertion with PET idle, mean B1+ of  $46.0 \mu\text{T} \pm 11.2\%$ ; and (c) with PET acquiring, mean B1+ of  $46.1 \mu\text{T} \pm 11.1\%$ . (d) Difference between maps acquired with and without PET acquisition.

TABLE V  
RESULTS FROM FBIRN TEST.

	<i>PET Idle</i>		<i>PET Acquiring</i>		<i>MR750w</i>	
	Mean	Std	Mean	Std	Mean	Std
<b>HNU Receive Coil</b>						
<b>RMS (%)</b>	0.035	0.002	0.034	0.003	0.037	0.006
<b>P-2-P (%)</b>	0.20	0.03	0.18	0.03	0.22	0.06
<b>SFNR</b>	830	17	832	2	813	15
<b>SNR</b>	893	46	851	59	851	4
<b>Body Receive Coil</b>						
<b>RMS (%)</b>	0.043	0.001	0.042	0.002	0.072	0.0002
<b>P-2-P (%)</b>	0.21	0.02	0.21	0.02	0.44	0.05
<b>SFNR</b>	328	4	323	3	225	19
<b>SNR</b>	346	25	336	9	242	3

difference between  $B_1$  + of RF Body coil with and without PET acquisition is about 0.3%, which is practically insignificant.

Table V shows the comparison of FBIRN test results between the 3 modes using the Body coil and HNU coil as receive coil. It shows that the RF body coil stability and SNR and SFNR both are improved by  $> 40\%$  in PET/MR compared to MR750w.

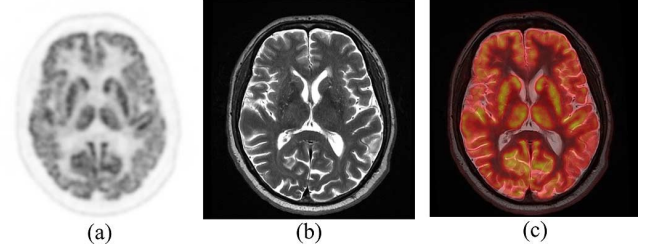


Fig. 10. Axial brain images: (a) PET image from TOF PET/MR system; (b) PET/MR FRFSE image and (c) PET/MR co-registered image.

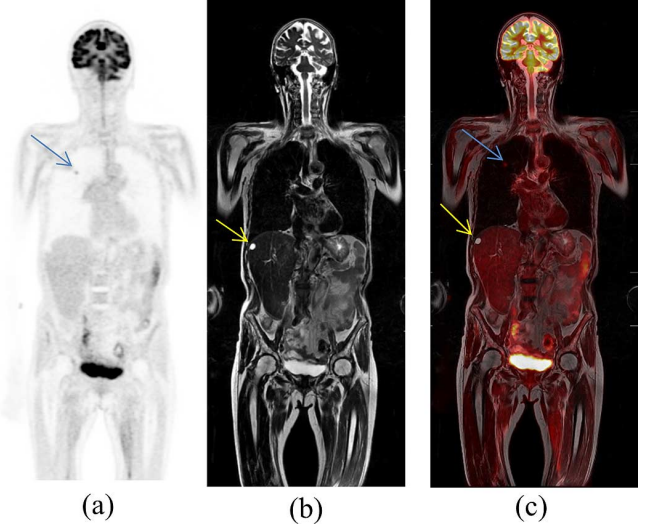


Fig. 11. Coronal whole-body images of the second subject with lesions in lung and liver regions as pointed by the arrows. Shown are (a) PET image from TOF PET/MR system; (b) MR coronal image; and (c) co-registered PET+MR images.

The head-neck unit shows similar stability results. The differences in stability (RMS) and SFNR were  $< 3\%$  and  $< 0.3\%$  for both coils between no PET acquisition mode and PET acquiring mode, respectively; however, SNR is 3–4% lower in PET acquiring mode compared to PET powered but idle mode.

### C. Clinical Study

Fig. 10 shows an example of axial brain images acquired on the TOF PET/MR system. There were no visible artifacts in the simultaneously acquired images. Fig. 11 shows coronal whole-body images obtained from the PET/MR system.

## IV. DISCUSSION

In this work we presented the design and performance measurements of the GE SIGNA PET/MR with TOF capability. This hybrid scanner was built with a novel RF body coil designed to accommodate a PET ring without compromising MR image quality. The tests and experiments performed and presented in this paper were on a prototype system that is equivalent in design and performance to the commercially available SIGNA PET/MR. Analog SiPM-based PET detectors were employed for the first time in a clinical whole body system, providing high resolution PET images with TOF capability in a harsh MR environment. The SiPM devices were regulated for thermal drift by a continuously running gain compensation

mechanism. With the temperature compensation enabled, the ratio of the normalized coincidence count rate remains steady with and without MR stimulus. We observed residual drifts that have negligible impact for the purposes of PET image quantitation (Fig. 4).

Performance test results indicate insignificant mutual interference between the two sub-systems (Figs. 6–8). The mean PET system energy resolution and coincidence timing resolution outside and inside the magnet were degraded by  $< 2\%$ , and  $< 3\%$ , respectively (Fig. 5 and Table III). Though RF-induced noise degraded the timing resolution by roughly 10 ps for the FRFSE sequence, this corresponds to  $< 1\%$  shift in timing trigger threshold and has minimal to no impact on system performance. Therefore, this degradation is insignificant for clinical applications. The timing resolution measurement performed with decaying  $^{18}\text{F}$  activity shows a linear relationship (to within 0.3%) of resolution with activity (Fig. 5). Over the typical activity range expected in routine clinical use, this degradation in timing resolution is minimal. Moreover, excellent timing resolution of  $< 400$  ps enables high quality TOF reconstruction of PET images with sharp contrast (Figs. 8, 10 and 11). Preliminary PET evaluation using image quality phantom with MR idle and active MR pulsing indicates no significant image artifacts (Fig. 8).

Our evaluation of mutual interference also indicated that the effects of the PET ring integrated inside MR system on MR performance were minimal (Tables IV and V). Although minor differences in measured MR image SNR values were seen; such differences could be compensated by a small increase ( $< 10\%$ ) in acquisition time, but are at any rate not expected to have relevance for MRI studies. Similarly, from Tables IV and V we observed no significant inhomogeneity in either the static ( $B_0$ ) or the radiofrequency ( $B_1$ ) fields of the MR system in the presence of PET detector electronics.

Similar  $B_1$  uniformity results before and after PET ring insertion indicate that MR image uniformity and contrast stays the same, while higher  $B_1$  field, allows the use of shorter RF pulses in MR imaging. In addition to being closer to the system center, the PET/MR body coil is more efficient in terms of generating the same  $B_1$  field with less RF power. As a result, the E-fields near the body coil will be lower and this reduces peak SAR compared to MR750w.

Since the main goal of this paper is to highlight novel design features of the integrated system and study the mutual compatibility, measurements on PET data quantification and detailed PET NEMA NU 2-2012 performance measurements have been studied in a separate paper [18]. The differences in contrast recovery and percent background variability were minimal for various sizes of the spheres with MR idle and MR active conditions (e.g.,  $< 0.5\%$  for 17 mm sphere). In addition, the lung residual error is  $< 4\%$ . With TOF capability, it is now possible to minimize PET quantification bias substantially and significantly improve the quantitative accuracy of standard MRAC methods [30]. In addition, the TOF non-attenuation corrected images provide better patient boundary [22], [24], when compared to using non-TOF data for truncation completion as was reported elsewhere [31]. Furthermore, the results of MR performance before and after PET insertion were also reported

[32]. Clinical evaluation of the PET/MR system was recently reported in a study comparing PET/CT and PET/MR data from the same set of patients, highlighting excellent PET image quality achieved with the new technology [19]. PET and MR brain and whole-body images shown in Figs. 10 and 11, respectively, were simultaneously acquired and show complementary morphology and functional information. The lesions in both lung and liver were visible in the fused image, but could have been missed on a standalone modality.

In summary, the GE SIGNA PET/MR system with TOF capability shows great promise to provide comparable or superior imaging performance for complex clinical applications in comparison to the case that the two systems are separate. Further work will involve exploring applications in fMRI/PET functional imaging techniques.

## V. CONCLUSION

This paper presented design details and results from tests of mutual compatibility for a simultaneous TOF-PET/MR system. The results indicate that the system is capable of excellent performance during simultaneous PET/MR without significant mutual interference.

## ACKNOWLEDGMENT

The authors would like to thank University Hospital Zurich for providing clinical images and support during this study; F. Chin and B. Shen at Stanford Radiochemistry Facility; and W. T. Peterson, C. Kim, D. McDaniel and C. Bobb at GE Healthcare, for their support during PET/MR performance measurements and data analysis.

## REFERENCES

- [1] G. Delso and S. Ziegler, "PET/MRI system design," *Eur. J. Nucl. Med. Mol. Imag.*, vol. 36, pp. S86–92, 2009.
- [2] B. J. Pichler, A. Kolb, T. Nagele, and H. P. Schlemmer, "PET/MRI: Paving the way for the next generation of clinical multimodality imaging applications," *J. Nucl. Med.*, vol. 51, pp. 333–6, 2010.
- [3] Y. Shao *et al.*, "Simultaneous PET and MR imaging," *Phys. Med. Biol.*, vol. 42, pp. 1965–70, 1997.
- [4] J. E. Mackewn *et al.*, "Performance evaluation of an MRI-compatible pre-clinical PET system using long optical fibers," *IEEE Trans. Nucl. Sci.*, vol. 57, no. 3, pp. 1052–1062, Jun. 2010.
- [5] N. L. Christensen, B. E. Hammer, B. G. Heil, and K. Fetterly, "Positron emission tomography within a magnetic field using photomultiplier tubes and lightguides," *Phys. Med. Biol.*, vol. 40, pp. 691–7, 1995.
- [6] B. J. Pichler *et al.*, "Performance test of an LSO-APD detector in a 7-T MRI scanner for simultaneous PET/MRI," *J. Nucl. Med.*, vol. 47, pp. 639–47, 2006.
- [7] S. H. Maramraju *et al.*, "Small animal simultaneous PET/MRI: Initial experiences in a 9.4 T microMRI," *Phys. Med. Biol.*, vol. 56, pp. 2459–80, 2011.
- [8] S. J. Hong *et al.*, "SiPM-PET with a short optical fiber bundle for simultaneous PET-MR imaging," *Phys. Med. Biol.*, vol. 57, pp. 3869–83, 2012.
- [9] N. F. Schwenzer *et al.*, "Simultaneous PET/MR imaging in a human brain PET/MR system in 50 patients—Current state of image quality," *Eur. J. Radiol.*, vol. 81, pp. 3472–8, 2012.
- [10] G. Delso *et al.*, "Performance measurements of the Siemens mMR integrated whole-body PET/MR scanner," *J. Nucl. Med.*, vol. 52, pp. 1914–22, 2011.
- [11] H. Zaidi *et al.*, "Design and performance evaluation of a whole-body Ingenuity TF PET-MRI system," *Phys. Med. Biol.*, vol. 56, pp. 3091–106, 2011.
- [12] P. Veit-Haibach, F. P. Kuhn, F. Wiesinger, G. Delso, and G. von Schulthess, "PET-MR imaging using a tri-modality PET/CT-MR system with a dedicated shuttle in clinical routine," *MAGMA*, vol. 26, pp. 25–35, 2013.

- [13] M. Conti, "State of the art and challenges of time-of-flight PET," *Phys. Med.*, vol. 25, pp. 1–11, 2009.
- [14] J. S. Karp, S. Surti, M. E. Daube-Witherspoon, and G. Muehllehner, "Benefit of time-of-flight in PET: Experimental and clinical results," *J. Nucl. Med.*, vol. 49, pp. 462–70, 2008.
- [15] W. W. Moses, "Time of flight in PET revisited," *IEEE Trans. Nucl. Sci.*, vol. 50, no. 5, pp. 1325–1330, Oct. 2003.
- [16] D. R. Schaart *et al.*, "LaBr(3):Ce and SiPMs for time-of-flight PET: Achieving 100 ps coincidence resolving time," *Phys. Med. Biol.*, vol. 55, pp. N179–89, 2010.
- [17] J. Y. Yeom, R. Vinke, and C. S. Levin, "Optimizing timing performance of silicon photomultiplier-based scintillation detectors," *Phys. Med. Biol.*, vol. 58, pp. 1207–20, 2013.
- [18] A. M. Grant *et al.*, "NEMA NU 2-2012 performance studies for the SiPM-based ToF-PET component of the GE SIGNA PET/MR system," *Med. Phys.*, vol. 43, pp. 2334–2343, 2016.
- [19] A. Iagaru *et al.*, "Simultaneous whole-body time-of-flight 18F-FDG PET/MRI: A pilot study comparing SUVmax with PET/CT and assessment of MR image quality," *Clin. Nucl. Med.*, vol. 40, pp. 1–8, 2015.
- [20] A. A. Wagadarikar, A. Ivan, S. Dolinsky, and D. L. McDaniel, "Sensitivity improvement of time-of-flight (ToF)-PET detector through recovery of Compton scattered annihilation photons," *IEEE Trans. Nucl. Sci.*, vol. 61, pp. 121–125, 2014.
- [21] C. Kim, W. T. Peterson, T. Kidane, S. H. Maramraju, and C. S. Levin, "Compensation for thermally-induced loads on PET detectors from MR stimulus in simultaneous PET/MR imaging," presented at the ISMRM, Milan, Italy, 2014.
- [22] S. D. Wollenweber *et al.*, "Comparison of 4-class and continuous fat/water methods for whole-body, MR-based PET attenuation correction," *IEEE Trans. Nucl. Sci.*, vol. 60, no. 5, pp. 3391–3398, Oct. 2013.
- [23] S. D. Wollenweber *et al.*, "Evaluation of an atlas-based PET head attenuation correction using PET/CT and MR patient data," *IEEE Trans. Nucl. Sci.*, vol. 60, no. 5, pp. 3383–3390, Oct. 2013.
- [24] H. Qian, R. M. Manjeshwar, S. Ambwani, and S. D. Wollenweber, "Truncation completion of MR-based PET attenuation maps using time-of-flight non-attenuation-corrected PET images," in *IEEE Nucl. Sci. Symp. Conf. Rec.*, 2012, pp. 2773–2775.
- [25] Performance measurements of positron emission tomographs NEMA Standards Publication, NU 2-2012, 2012, .
- [26] G. H. Glover *et al.*, "Function biomedical informatics research network recommendations for prospective multicenter functional MRI studies," *J. Magn. Reson. Imag.*, vol. 36, pp. 39–54, 2012.
- [27] T. Schirmer and D. P. Auer, "On the reliability of quantitative clinical magnetic resonance spectroscopy of the human brain," *NMR Biomed.*, vol. 13, pp. 28–36, 2000.
- [28] M. M. Khalighi, B. K. Rutt, and A. B. Kerr, "Adiabatic RF pulse design for Bloch-Siegert B+ mapping," *Magn. Reson. Med.*, vol. 70, pp. 829–835, 2013.
- [29] A. M. Alessio *et al.*, "Application and evaluation of a measured spatially variant system model for PET image reconstruction," *IEEE Trans. Med. Imag.*, vol. 29, pp. 938–49, 2010.
- [30] A. Mehranian and H. Zaidi, "Impact of time-of-flight PET on quantification errors in MR imaging-based attenuation correction," *J. Nucl. Med.*, vol. 56, pp. 635–41, Apr. 2015.
- [31] J. Nuyts *et al.*, "Completion of a truncated attenuation image from the attenuated PET emission data," *IEEE Trans. Med. Imag.*, vol. 32, no. 2, pp. 237–46, Feb. 2013.
- [32] M. M. Khalighi *et al.*, "MR performance comparison of a PET/MR system before and after SiPM-based time-of-flight PET detector insertion," *IEEE Trans. Nucl. Sci.*, 2016, to be published.